

RESEARCH LETTER

10.1029/2018GL079025

Special Section:

Curiosity at the Bagnold Dunes, Gale crater: Advances in Martian eolian processes

Key Points:

- Bagnold Phase 2 sands exhibit higher 535-nm band depths and red/blue ratios and lower 600-/700-nm ratios than Bagnold Phase 1 sands
- Phase 2 sands contain a greater amount of redder, ferric materials, likely owing to minor hematite contamination from nearby bedrock

Supporting Information:

- Supporting Information S1

Correspondence to:

J. R. Johnson,
jeffrey.r.johnson@jhuapl.edu

Citation:

Johnson, J. R., Bell, J. F., III, Bender, S., Cloutis, E., Ehlmann, B., Fraeman, A., et al. (2018). Bagnold Dunes campaign phase 2: Visible/near-infrared reflectance spectroscopy of longitudinal ripple sands. *Geophysical Research Letters*, 45, 9480–9487. <https://doi.org/10.1029/2018GL079025>

Received 31 MAY 2018

Accepted 13 JUL 2018

Accepted article online 23 JUL 2018

Published online 27 SEP 2018

Bagnold Dunes Campaign Phase 2: Visible/Near-Infrared Reflectance Spectroscopy of Longitudinal Ripple Sands

Jeffrey R. Johnson¹ , James F. Bell III² , Steve Bender³, Edward Cloutis⁴ , Bethany Ehlmann^{5,6} , Abigail Fraeman⁵ , Olivier Gasnault⁷ , Sylvestre Maurice⁷, Patrick Pinet⁷ , Lucy Thompson⁸ , Danika Wellington², and Roger C. Wiens⁹ 

¹The Johns Hopkins University Applied Physics Laboratory, Laurel, MD, USA, ²School of Earth and Space Exploration, Arizona State University, Tempe, AZ, USA, ³Planetary Science Institute, Tucson, AZ, USA, ⁴Department of Geography, University of Winnipeg, Winnipeg, Manitoba, Canada, ⁵Jet Propulsion Laboratory, Pasadena, CA, USA, ⁶Division of Geological and Planetary Sciences, California Institute of Technology, Pasadena, CA, USA, ⁷CNRS, Institut de Recherche en Astrophysique et Planetologie, Université de Toulouse, Toulouse, France, ⁸Department of Earth Sciences, University of New Brunswick, Fredericton, New Brunswick, Canada, ⁹Los Alamos National Laboratory, Los Alamos, NM, USA

Abstract As part of the Phase 2 Bagnold Dune campaign at Gale Crater, Mars, constraints on the geochemistry, mineralogy, and oxidation state of pristine and disturbed linear sand ripples were made using visible/near-infrared spectral observations for comparison to Phase 1 spectra of the barchan dunes to the north. Spectra acquired by the ChemCam and Mastcam instruments (400–1,000 nm) at four Phase 2 locations revealed similar overall spectral trends between the two regions, but most Phase 2 sands were redder in the visible wavelengths. The majority of targets exhibited lower red/infrared ratios, higher ~530-nm band depths, and higher red/blue ratios than Phase 1 samples, suggesting a greater proportion of redder, fine-grained, ferric sands in Phase 2 samples. This is consistent with the slightly greater proportion of hematite in Phase 2 samples as determined from CheMin analyses of the Ogunquit sands, which may reflect contamination from the surrounding hematite-bearing Murray formation bedrock.

Plain Language Summary The Mars Science Laboratory Curiosity rover visited the southern portion of the Bagnold Dunes to look for differences in the types of sand grains that comprised the dunes and ripples. The rover's cameras and spectrometers provided information about the color of the sands, which was used to infer the composition and types of minerals. Overall, the sands in this part of the Bagnold Dunes were a bit redder than those further to the north that were studied previously. We interpreted this to mean that the southern sands contained more oxidized (rusted) iron particles. Because the rocks surrounding these dunes were known to contain a fair amount of red, iron-rich minerals, it is probable that the sands were mixed with a small amount of broken fragments from these rocks.

1. Introduction

Understanding the provenance and evolution of windblown sands on Mars requires a combination of regional and local analyses of their geochemical and mineralogical diversity. During Phase 1 of the Bagnold Dune campaign conducted by the Mars Science Laboratory Curiosity (Sols 1,181–1,254) the barchan dunes in the Namib and High Dune areas were investigated (Bridges & Ehlmann, 2018; Ehlmann et al., 2017). Phase 2 of the campaign (Sols 1,601–1,653) studied ripple fields and linear dunes in the Mount Desert Island and Nathan Bridges Dune regions 2 km to the south and ~100 m higher in elevation (Lapôtre & Rampe, 2018). Both campaigns acquired visible/near-infrared (400–1,000 nm) reflectance spectra of pristine, disturbed, and sieved sands using Mast Camera (Mastcam) multispectral imaging (445–1,013 nm) and Chemistry and Camera (ChemCam) passive point spectroscopy (400–840 nm). Johnson et al. (2017) reported that the Phase 1 dune sands were distinct from other Martian dusty sands and typically exhibited low relative reflectance, weak ~530-nm absorption bands, an absorption band near 620 nm, and a decrease in spectral reflectance longward of ~685 nm. These characteristics were consistent with dominantly olivine-bearing sands, with likely contributions from high-calcium pyroxene (cf. Lapôtre et al., 2017). However, variations were observed between the finer- and coarser-grained sands. Fine sands exhibited higher 535-nm absorption band depths and lower 600-/700-nm spectral ratios, consistent with a combination of ferric materials (e.g., hematite, magnetite, nanophase, and/or amorphous oxides). Conversely, the coarsest grains (in ridge



Figure 1. High Resolution Imaging Science Experiment (HiRISE) orbital color scene of Phase 2 region, showing rover traverse (white) and four stops made during the campaign. Background image is HiRISE ESP_035772_1755.

crests and lee slopes) were the darkest and bluest, with strong reflectance downturns in the near-infrared, higher 600-/700-nm ratios (flatter spectra in this region) and near-zero 535-nm band depths, consistent with greater proportions of mafic silicate minerals.

We report here analyses of Mastcam and ChemCam reflectance data acquired during the Phase 2 campaign, which comprised four stops along the rover traverse (Figure 1). The first three of these stops (Mapleton, Sandy Point Beach, and Southern Cove) sampled locations on the eastern margin of Nathan Bridges Dune (Figures S1–S4 in the supporting information). The fourth stop was on the western edge of Mount Desert Island at Ogunquit Beach (Figure S5), where scooped sands were sieved for onboard analyses (Rampe et al., 2018; Stern et al., 2018). The presieved ($>150\text{ }\mu\text{m}$) and postsieved ($<150\text{ }\mu\text{m}$) samples were kept onboard the rover until they were dumped on Sol 1,968 and analyzed with Mastcam and ChemCam shortly thereafter (Figure S6).

2. Methodology

2.1. ChemCam Passive Spectra

The ChemCam instrument is used for laser-induced breakdown spectroscopy (LIBS) in which light from a laser-generated plasma is dispersed onto three spectrometers to detect elemental emission lines at high spectral resolution ($<1\text{ nm}$; Wiens et al., 2013, 2015). Relative reflectance spectra (400–840 nm) can be collected in passive mode (i.e., without using the laser) for each sunlit location to provide information on variations in ferrous and ferric components (Johnson et al., 2015, 2016, 2017). For materials near the rover ($\sim 2\text{--}7\text{ m}$) the 0.65-mrad field of view of each point measurement sampled areas 1.3–4.5 mm. Each LIBS measurement included a 3-ms exposure passive (*dark*) measurement used to subtract ambient light from the LIBS spectrum. Because the laser shock wave creates pits in the sands, passive measurements shown here were acquired prior to its use to avoid pit shadows. Passive measurements at 30-ms exposures were acquired for specific targets to increase the signal-to-noise ratio. Data acquired on Sol 76 at 12:52 LTST of the white ChemCam calibration target holder were used to minimize dark current variations between scene and calibration targets. Raw data were converted to radiance (Johnson et al., 2015), with an estimated absolute 6–8% calibration uncertainty. The ratio of the scene and Sol 76 calibration target radiance was multiplied by the laboratory reflectance of the calibration target material (Wiens et al., 2012) to provide relative reflectance. Images from the Remote Micro-Imager were acquired to provide accurate positions for raster locations (Le Mouélic et al., 2015; Maurice et al., 2012, 2016; Wiens et al., 2012, 2015; Figure S6).

We calculated spectral parameters using ± 5 -nm averages around a central wavelength. Near-infrared ratios (e.g., 600/700 nm) and peak reflectance wavelengths are indicative of the strength of iron absorptions from mafic minerals, and 600-/440-nm (red/blue) ratios are sensitive to oxidation state and/or dust deposition. The 535-nm band depth (calculated using shoulders at 500 and 600 nm) is sensitive to the presence of crystalline ferric oxides (e.g., Bell et al., 2000; Morris et al., 1997, 2000).

2.2. Mastcam Passive Spectra

The Mastcam system includes two cameras (M100, 100-mm focal length and M34, 34-mm focal length) that use $1,600 \times 1,200$ pixel Bayer-patterned CCDs. Each uses six narrow band (± 10 nm) filters to characterize the 445- to 1,013-nm reflectance spectra of surface targets. One filter position has a broadband infrared-cut off filter for RGB color imaging using a Bayer pattern bonded directly to the detectors (Wellington et al., 2017). The two cameras provide 12 center wavelengths for multispectral analysis, including the three RGB Bayer bands (which have ± 40 -nm bandwidths). Wellington et al. (2017) and Bell et al. (2003, 2017) describe conversion of raw Mastcam data to radiance ($\text{W}/\text{m}^2/\text{nm}/\text{sr}$) and to radiance factor (I/F) using observations of the onboard Mastcam calibration target (Bell et al. 2003; He et al. 1991; Kinch et al., 2015; Wellington et al., 2017). Radiance factors were divided by the cosine of the solar incidence angle to provide relative reflectance (R^*), an approximation of the reflectance factor defined in Hapke (1993, 2012). Relative reflectance spectra presented here are average values derived from manually defined regions selected of the same region in the M34 and M100 images. M100 filter values were scaled to the left eye at the 1,013-nm wavelength (which is least affected by uncertainties in the dust correction) and averaged with the M34 values at overlapping wavelengths to produce a combined spectrum. The absolute radiometric accuracy for Mastcam is estimated to be 10–20%, with a filter-to-filter uncertainty of $<5\%$ and pixel-to-pixel variation of $<1\%$ (Bell et al. 2003, 2017; Wellington et al. 2017).

Mastcam spectral parameters were calculated using wavelengths similar to the ChemCam spectral parameters. Parameters sensitive to ferric crystallinity, oxidation state, and/or dust deposition included the band depth at 527 nm (calculated using shoulders at 494 and 639 nm), the peak reflectance position, and the 639-/446-nm ratio. Near-infrared parameters (676-/751-nm ratio) are sensitive to mafic silicate minerals.

3. Data Sets Used

Table 1 lists the ChemCam and Mastcam data sets acquired at each Stop that were used in this analysis. At Stop 1, Mastcam observations were acquired of undisturbed and Alpha Particle X-Ray Spectrometer (APXS)-disturbed ripple sands at Matagamon and two locations on pristine and rover wheel-disturbed sands in the Scarboro area (Figures S1 and S2). ChemCam data were acquired at Mapleton. At Stop 2, Mastcam imaging at Macworth documented rover tracks and pristine sands (Figure S3), while ChemCam observations sampled the edge of a rover track (Macworth) and ripple crests (Towow, Leighton, Carrassett, and Swanback). Between Stops 2 and 3 ChemCam observed the ripple crest Mattawamkeag. At Stop 3, Mastcam targeted the pristine and disturbed sands at Hildreths (Figure S4), while ChemCam observed disturbed sands at Greenvale Cove and the ripple crests Ripogenus (Figure S7) and Spragueville (acquired twice owing to shadows obscuring raster locations 7–10 during the first attempt). At Stop 4, Mastcam observed pristine and rover-disturbed sands near Ogunquit (Figure S5), and ChemCam acquired spectra on a rover scuff wall (Tumbledown Mountain), the base of that wall (Elephant Mountain), and on the scuff floor (Canoe Point). Undisturbed sand was observed at North Brother, and ripple crests of different sizes were sampled at Hamlin Peak (small), Avery Peak (medium), and Baxter Peak (large; Figure S7). Unused portions of the Ogunquit sand samples were kept onboard until Sol 1,970, when the postsieve ($<150 \mu\text{m}$) and presieve ($>150 \mu\text{m}$) samples were dumped onto bedrock while the rover was on Vera Rubin Ridge and analyzed by Mastcam and using dedicated passive and active ChemCam methods (Figures S6 and S8–S10).

4. Results

4.1. ChemCam and Mastcam Spectra

Representative Chemcam passive and Mastcam relative reflectance spectra from the four stops are shown in Figure 2. Spectral differences among disturbed, undisturbed, and ripple crest/trough sands are marked by

Table 1
ChemCam and Mastcam Sequences Used

Target	Stop no.	Sol	Sequence ID	LTST (start)	Raster size column × row
Mapleton	1	1,602	ccam1602	12:11	5 × 1
New Sweden	2	1,617	ccam1617	10:26	1 × 5
Macworth	2	1,618	ccam3618	10:44	1 × 10
Towow	2	1,618	ccam1618	10:18	5 × 1
Leighton	3	1,623	ccam2623	12:30	10 × 1
Carrasett	3	1,625	ccam1625	11:43	10 × 1
Swanback	3	1,627	ccam1627	11:42	1 × 10
Mattawamkeag	2/3	1,630	ccam2630	12:45	1 × 5
Ripogenus	3	1,637	ccam2637	10:35	1 × 10
Spragueville	3	1,637	ccam1637	10:06	1 × 10
Spragueville_2	3	1,638	ccam2638	12:12	1 × 10
Greenvale Cove	3	1,639	ccam1639	11:49	1 × 7
Tumbledown Mountain	4	1,652	ccam1652	11:18	5 × 1
Elephant Mountain	4	1,652	ccam2652	11:32	5 × 1
Canoe Point	4	1,652	ccam3652	11:48	5 × 1
North Brother	4	1,653	ccam1653	11:04	5 × 1
Avery Peak	4	1,653	ccam2653	11:19	10 × 1
Baxter Peak	4	1,653	ccam3653	14:15	10 × 1
Ogunquit postsieve passive	—	1,970	ccam5968	12:27	5 × 1
Ogunquit presieve passive	—	1,971	ccam1971	13:24	5 × 1
Ogunquit postsieve active	—	1,971	ccam2971	13:33	5 × 1
Ogunquit presieve active	—	1,972	ccam1972	12:53	5 × 1
Matagamon	1	1,603	mcam08177	12:40	—
Scarboro	1	1,603	mcam08179	12:50	—
Macworth	2	1,618	mcam08273	11:28	—
Hildreths	3	1,637	mcam08465	11:12	—
Ogunquit	4	1,652	mcam08558	10:50	—
Ogunquit dump	—	1,970	mcam10306	12:07	—

Note. LTST = Local True Solar Time.

changes in the visible spectral slope, maximum reflectance position, and the steepness of the near-infrared slope. These are due to variations in the relative abundance and/or grain size of mafic minerals (olivines and pyroxenes) versus finer-grained, more ferric, oxidized materials, particularly in the disturbed sands, modulated by the effects of amorphous components (e.g., Achilles et al., 2017; Rampe et al., 2018). In the

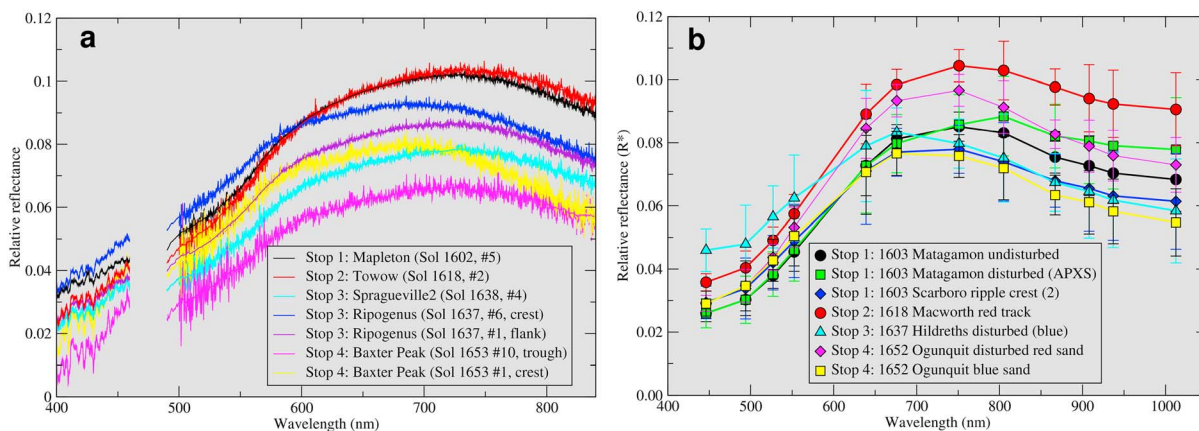


Figure 2. (a) ChemCam passive reflectance spectra of representative samples acquired at the four stops of the Phase 2 campaign. Legend shows Sol number and raster location number in parentheses. Gap between 468 and 478 nm represents region between ChemCam detectors. Each spectrum includes a 50-channel average line overlaid; only this average is shown in the 400- to 500-nm region owing to low SNR in this region. (b) Mastcam relative reflectance spectra of representative samples acquired at the four stops. Error bars represent standard deviation of region of interest selected (see Figures S1–S5 for locations from which spectra were extracted). APXS = Alpha Particle X-Ray Spectrometer; SNR = signal-to-noise ratio.

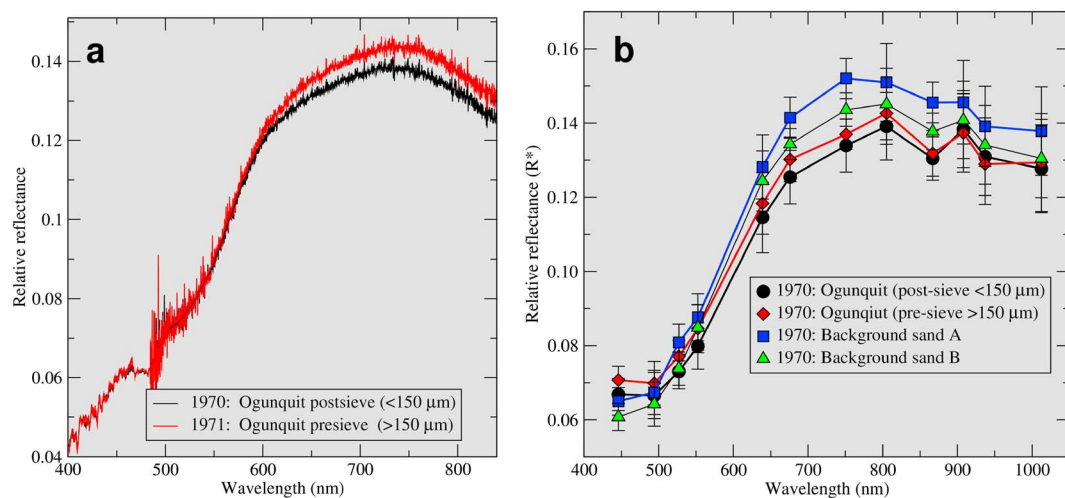


Figure 3. (a) ChemCam passive reflectance spectra of Ogunquit presieved ($150 > \mu\text{m}$) and postsieved ($<150 \mu\text{m}$) dumped samples. (b) Mastcam relative reflectance spectra of Ogunquit dumped samples (extracted from same area sampled by ChemCam raster, cf. Figure S6) compared to spectra of background sands in the same scene.

Mapleton and Towow areas, ChemCam spectra are typical of reddish sands observed elsewhere throughout the traverse (Johnson et al., 2015, 2016). The crest of the Ripogenus ripple exhibited reflectance maxima at shorter wavelengths than the flank, consistent with more ferrous materials on the crest (cf. Figure S7). The spectral shapes of nearby Spragueville sands were nearly identical to the Ripogenus flank. The Baxter Peak ripple target's crest showed the strongest near-infrared downturn, consistent with more ferrous sands compared to the trough (cf. Figure S7). In enhanced Mastcam color images, the coarser disturbed sands in the Hildreths area appear bluish (Figure S4). The corresponding Mastcam spectra in Figure 2b show a maximum reflectance near 675 nm compared to a maximum reflectance position near 750 nm associated with redder sands of Macworth and Ogunquit. Similar shorter-wavelength maxima were observed for bluer regions at the Ogunquit area and the ripple crest target Scarboro in the Mapleton area. For comparison, redder sands in the troughs of scuff areas and flanks of ripples in the Scarboro area exhibited longer-wavelength maxima. In summary, ripple crests (e.g., Ripogenus, Baxter Peak, and Scarboro) and collections of coarser grains in disturbed soils (e.g., Hildreths and Ogunquit) tend to exhibit reflectance peaks at shorter wavelengths, steeper near-infrared downturns, and weak to nonexistent ~ 530 -nm band depths, consistent with more ferrous materials compared to the redder, more ferric ripple flanks or troughs.

The Ogunquit presieve and postsieve dumped samples exhibited very similar ChemCam passive and Mastcam relative reflectance spectra (Figures 3 and S6), with ~ 530 - and 867-nm absorption bands in both samples. Nearby background sand exhibited similar Mastcam spectra, albeit with some variations in the strength of the 867-nm band. This is evident in the Mastcam 867-nm band depth image (Figure S8) in which the dumped samples and background sands are essentially indistinguishable. However, the 527-nm band depth images showed that the dumped samples were slightly brighter than the background sands (Figures S8–S10), and the decorrelation stretch images manifest this with more purple hues in the dump piles. This spectral behavior suggests a greater proportion of ferric oxides in the Ogunquit sieved sands. Rampe et al. (2018) discuss the possible contamination of this sample by remnants of the previously drilled, hematite-rich sample Sebina. However, they did not estimate hematite contamination and concluded from Chemistry and Mineralogy (CheMin) data that minor (1.2 wt%) hematite is likely present in the crystalline + amorphous portion of the Ogunquit $<150\text{-}\mu\text{m}$ sample.

4.2. Spectral Parameters

Spectral parameters computed from ChemCam spectra are shown in Figure 4, where the 600-/700-nm (red/infrared) ratio is compared to the 535-nm band depth and 600-/440-nm (red/blue) ratio. Parameters from representative Phase 1 targets are shown for comparison (square symbols). Phase 2 samples were redder

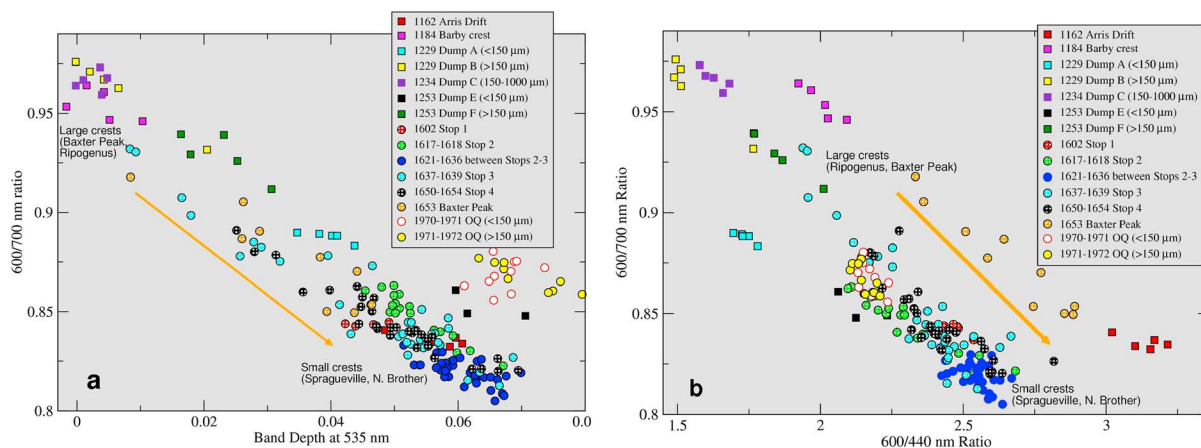


Figure 4. ChemCam spectral parameters for Phase 2 (circles) and representative Phase 1 samples (squares; cf. Johnson et al., 2017). (a) The 535-nm band depth versus 600-/700-nm ratio. (b) The 600-/440-nm ratio versus 600-/700-nm ratio. Orange arrow points from coarser, more ferrous sands on larger ripple crests to finer, more ferric sands on smaller ripple crests.

(higher 600-/440-nm ratios) than most Phase 1 samples, with lower red/near-infrared ratios. Exceptions were the bluer portions of ripple crests with higher red/infrared ratios (e.g., Baxter Peak and Ripogenus), which transitioned into redder, more ferric materials along the flanks or troughs of the ripples, as shown schematically by the orange arrows in Figure 4. The Ogunquit dump samples exhibited high 535-nm band depths but were among the least red Phase 2 samples, similar to the Dump E ($< 150 \mu\text{m}$) sands from Phase 1.

Figure 5 shows similar spectral parameters computed from Mastcam spectra from both campaign phases, where the 676-/751-nm (red/infrared) ratio is compared to the 527-nm band depth and the 639/446 (red/blue) ratio. Nearly all Phase 2 samples were redder with stronger 527-nm band depths than Phase 1 sands, with low red/infrared ratios closer to the $< 150\text{-}\mu\text{m}$ Phase 1 sieved samples. The exceptions were the bluer, coarser disturbed sands from Hildreths, Ogunquit, and Matagamon, which exhibited the weakest 527-nm band depths and highest red/infrared ratios, transitioning to finer, redder sands as shown schematically by the arrows (cf. Figures S1–S5). The Ogunquit samples were much less red than other Phase 2 samples and most similar to Phase 1 sands. However, their 527-nm band depths and red/infrared ratios were similar to the other Phase 2 sands.

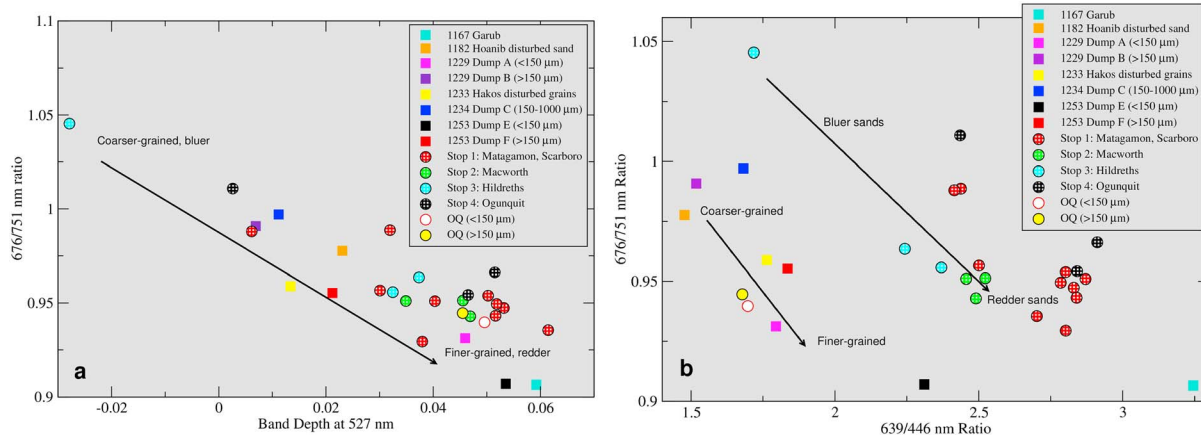


Figure 5. Mastcam spectral parameters for Phase 2 (circles) and representative Phase 1 samples (squares; cf. Johnson et al., 2017). (a) The 527-nm band depth versus 676-/751-nm ratio. (b) The 639-/446-nm ratio versus 676-/751-nm ratio. Black arrows point from coarser, bluer, more ferrous sands on larger ripple crests to finer, redder, more ferric sands on smaller ripple crests.

5. Discussion and Conclusions

Based on their higher ~530-nm band depths and red/blue ratios and lower red/infrared ratios, we interpret that most of the Phase 2 sands contained greater proportions of redder, fine-grained, ferric materials than Phase 1 sands. However, several of the bluer, coarser-grained Phase 2 ripple crests were similar to Phase 1 sands, and some exhibited higher red/infrared ratios for a given red/blue ratio than Phase 1 sands (e.g., Hildreths and Baxter Peaks' crest in Figure 5b). This likely resulted from the more active wind regime in this region (cf. Baker et al., 2018; Lapôtre et al., 2018), which limited dust contamination and exposed more ferrous sands. Indeed, APXS analyses suggested low dust content (implied from low S, Cl, and Zn concentrations), particularly for the more mafic ripple crests which contained relatively great amounts of Mg and Ni, compared to enrichments in Ti and Cr in off-crest sands (O'Connell-Cooper et al., 2018). By comparison, the sieved Ogunquit samples exhibited strong ~530-nm band depths but an overall less red appearance than other Phase 2 sands even though APXS analyses suggested higher dust contributions. We conclude that Phase 2 sands contained minor, detrital, hematite-rich particles sourced from the surrounding bedrock of the Murray formation in addition to relatively low proportions of mafic minerals. Analyses by Rampe et al. (2018) suggested lower olivine and higher plagioclase abundances in the crystalline portion of the <150- μm Ogunquit fraction than in the Phase 1 Gobabeb samples, along with ~2 wt% hematite. The proportion of crystalline hematite was likely larger in the Phase 2 sands, and/or the grain size distribution of hematite was smaller, in order to account for their stronger ~530-nm bands. In addition, images from the Mars Hand Lens Imager (MAHLI) suggested the presence of reddish outcrop fragments <500 mm in size, although the average grain size was smaller in the Phase 2 dune sands than Phase 1 (Weitz et al., 2018). Analyses of sands along the rest of the Curiosity rover traverse will continue to document compositional and mineralogical variations and potential bedrock contributions from the stratigraphy of Mount Sharp.

Acknowledgments

This work was funded by the NASA Mars Science Laboratory Participating Scientist program through the Jet Propulsion Laboratory (contracts 1350588 and 1546033). A portion of this research was carried out at JPL, under a contract with NASA. The U.S. portion of ChemCam and MSL rover operations was funded by NASA's Mars Exploration Program. The French contribution to MSL is supported by CNES. The authors thank the operations teams involved in acquiring these data sets and W. Farrand and an anonymous reviewer for their helpful comments. Original data that underlie the conclusions presented in this manuscript can be found on the NASA Planetary Data System and/or in the relevant references cited. The authors fondly recall the dedicated efforts toward the Bagnold Dune campaigns by our late colleague Nathan Bridges.

References

- Achilles, C. N., Downs, R. T., Ming, D. W., Rampe, E. B., Morris, R. V., Treiman, A. H., et al. (2017). Mineralogy of an active eolian sediment from the Namib dune, Gale crater, Mars. *Journal of Geophysical Research: Planets*, 122, 2344–2361. <https://doi.org/10.1002/2017JE005262>
- Baker, M. M., Lapotre, M. G. A., Minitti, M. E., Newman, C. E., Sullivan, R., Weitz, C. M., et al. (2018). The Bagnold Dunes in southern summer: Active sediment transport on Mars observed by the Curiosity rover. *Geophysical Research Letters*, 45. <https://doi.org/10.1029/2018GL079040>
- Bell, J. F. III, Godber, A., McNair, S., Caplinger, M. A., Maki, J. N., Lemmon, M. T., et al. (2017). The Mars science laboratory curiosity rover Mastcam instruments: Preflight and in-flight calibration, validation, and data archiving. *Earth and Space Science*, 4(7), 396–452. <https://doi.org/10.1002/2016EA000219>
- Bell, J. F. III, Squyres, S. W., Herkenhoff, K. E., Maki, J. N., Arneson, H. M., Brown, D., et al. (2003). Mars Exploration Rover Athena Panoramic Camera (Pancam) investigation. *Journal of Geophysical Research*, 108(E12), 8063. <https://doi.org/10.1029/2003JE002070>
- Bell, J. F., McSween, H. Y., Crisp, J. A., Morris, R. V., Murchie, S. L., Bridges, N. T., et al. (2000). Mineralogic and compositional properties of Martian soil and dust: Results from Mars Pathfinder. *Journal of Geophysical Research*, 105(E1), 1721–1755. <https://doi.org/10.1029/1999JE001060>
- Bridges, N. T., & Ehlmann, B. L. (2018). The Mars Science Laboratory (MSL) Bagnold Dunes campaign, Phase I: Overview and introduction to the special issue. *Journal of Geophysical Research: Planets*, 123, 3–19. <https://doi.org/10.1002/2017JE005401>
- Ehlmann, B. L., Ehlmann, B. L., Edgett, K. S., Sutter, B., Achilles, C. N., Litvak, M. L., et al. (2017). Chemistry, mineralogy, and grain properties at Namib and high dunes, Bagnold dune field, Gale crater, Mars: A synthesis of curiosity rover observations. *Journal of Geophysical Research: Planets*, 122, 2510–2543. <https://doi.org/10.1002/2017JE005267>
- Hapke, B. (1993). *Theory of reflectance and emittance spectroscopy* (p. 455). Cambridge: Cambridge University Press.
- Hapke, B. (2012). *Theory of reflectance and emittance spectroscopy* (2nd ed., p. 520). Cambridge: Cambridge University Press.
- He, X. D., Torrance, K. E., Sillion, F. X., & Greenberg, D. P. (1991). A comprehensive physical model for light reflection. *Proceedings of the 18th Annual Conference on Computer Graphics and Interactive Techniques*, 175–186.
- Johnson, J. R., Achilles, C., Bell, J. F. III, Bender, S., Cloutis, E., Ehlmann, B., et al. (2017). Visible/near-infrared spectral diversity from in situ observations of the Bagnold Dune Field sands in Gale Crater, Mars. *Journal of Geophysical Research*, 122, 2655–2684. <https://doi.org/10.1002/2016JE005187>
- Johnson, J. R., Bell, J. F. III, Bender, S., Blaney, D., Cloutis, E., DeFlores, L., et al. (2015). MSL science team, ChemCam passive reflectance spectroscopy of surface materials at the curiosity landing site, Mars. *Icarus*, 249, 74–92. <https://doi.org/10.1016/j.icarus.2014.02.028>
- Johnson, J. R., Bell, J. F. III, Bender, S., Blaney, D., Cloutis, E., Ehlmann, B., et al. (2016). Constraints on iron sulfate and iron oxide mineralogy from ChemCam visible/near-infrared reflectance spectroscopy of Mt. Sharp basal units, Gale Crater, Mars. *American Mineralogist*, 101(7), 1501–1514. <https://doi.org/10.2138/am-2016-5553>
- Kinch, K. M., Bell, J. F. III, Goetz, W., Johnson, J. R., Joseph, J., Madsen, M. B., & Sohl-Dickstein, J. (2015). Dust deposition on the decks of the Mars Exploration Rovers: 10 years of dust dynamics on the Panoramic Camera calibration targets. *Earth and Space Science*, 2(5), 144–172. <https://doi.org/10.1002/2014EA000073>
- Lapotre, M. G. A., & Rampe, E. B. (2018). Curiosity's investigation of the Bagnold Dunes, Gale crater: Overview of the two-phase scientific campaign and introduction to the special collection. *Geophysical Research Letters*, 45. <https://doi.org/10.1029/2018GL079032>

- Lapôtre, M. G. A., Ehlmann, B. L., Minson, S. E., Arvidson, R. E., Ayoub, F., Fraeman, A. A., et al. (2017). Compositional variations in sands of the Bagnold Dunes, Gale crater, Mars, from visible-shortwave infrared spectroscopy and comparison with ground truth from the Curiosity rover. *Journal of Geophysical Research: Planets*, 122, 2489–2509. <https://doi.org/10.1002/2016JE005133>
- Lapotre, M. G. A., Ewing, R. C., Weitz, C. M., Lewis, K. W., Lamb, M. P., Ehlmann, B. L., & Rubin, D. M. (2018). Morphologic diversity of Martian ripples: Implications for large-ripple formation. *Geophysical Research Letters*, 45. <https://doi.org/10.1029/2018GL079029>
- Le Mouélic, S., Gasnault, O., Herkenhoff, K. E., Bridges, N. T., Langevin, Y., Mangold, N., et al. (2015). The ChemCam remote micro-imager at Gale crater: Review of the first year of operations on Mars. *Icarus*, 249, 93–107. <https://doi.org/10.1016/j.icarus.2014.05.030>
- Maurice, S., Clegg, S. M., Wiens, R. C., Gasnault, O., Rapin, W., Forni, O., et al. (2016). ChemCam activities and discoveries during the nominal mission of Mars science laboratory in Gale crater, Mars. *Journal of Analytical Atomic Spectrometry*, 31(4), 863–889. <https://doi.org/10.1039/c5ja00417a>
- Maurice, S., Wiens, R. C., Saccoccia, M., Barracough, B., Gasnault, O., Forni, O., et al. (2012). The ChemCam instrument suite on the Mars Science Laboratory (MSL) rover: Science objectives and mast unit description. *Space Science Reviews*, 170(1–4), 95–166. <https://doi.org/10.1007/s11214-012-9912-2>
- Morris, R. V., Golden, D. C., & Bell, J. F. III (1997). Low-temperature reflectivity spectra of red hematite and the color of Mars. *Journal of Geophysical Research*, 102, 912–9133.
- Morris, R. V., Golden, D. C., Bell, J. F. III, Shetler, T. D., Scheinost, A. C., Hinman, N. W., et al. (2000). Mineralogy, composition, and alteration of Mars Pathfinder rocks and soils: Evidence from multispectral, elemental, and magnetic data on terrestrial analogue, SNC meteorite, and Pathfinder samples. *Journal of Geophysical Research*, 105(E1), 1757–1817. <https://doi.org/10.1029/1999JE001059>
- O'Connell-Cooper, C. D., Thompson, L. M., Spray, J. G., Berger, J. A., VanBommel, S. J., Gellert, R., et al. (2018). Chemical diversity of sands within the linear and barchan dunes of the Bagnold Dunes, Gale Crater, as revealed by APXS onboard Curiosity. *Geophysical Research Letters*, 45. <https://doi.org/10.1029/2018GL079026>
- Rampe, E. B., Lapotre, M. G. A., Bristow, T. F., Arvidson, R. E., Morris, R. V., Achilles, C. N., et al. (2018). Sand mineralogy within the Bagnold Dunes, Gale crater, as derived in situ and from orbit, this issue.
- Stern, J., Sutter, B., Archer, P. D., Eigenbrode, J. L., McAdam, A. C., Franz, H. B., et al. (2018). Major volatiles evolved from eolian materials in Gale crater. *Geophysical Research Letters*, 45. <https://doi.org/10.1029/2018GL079059>
- Weitz, C. M., Sullivan, R. J., Lapotre, M. G. A., Rowland, S. K., Grant, J. A., Baker, M., & Yingst, R. A. (2018). Sand grain sizes and shapes in eolian bedforms at Gale Crater, Mars. *Geophysical Research Letters*, 45. <https://doi.org/10.1029/2018GL078972>
- Wellington, D. F., Bell, J. F., Johnson, J. R., Kinch, K. M., Rice, M. S., Godber, A., et al. (2017). Visible to near-infrared MSL/Mastcam multispectral imaging: Initial results from select high-interest science targets within Gale Crater, Mars. *American Mineralogist*, 102(6), 1202–1217. <https://doi.org/10.2138/am-2017-5760CCBY>
- Wiens, R., Maurice, S., Barracough, B., Saccoccia, M., Barkley, W. C., Bell, J. F., et al. (2012). The ChemCam Instrument suite on the Mars Science Laboratory (MSL) Rover: Body unit and combined system performance. *Space Science Reviews*, 170(1–4), 167–227. <https://doi.org/10.1007/s11214-012-9902-4>
- Wiens, R. C., Maurice, S., Lasue, J., Forni, O., Anderson, R. B., Clegg, S., et al. (2013). Pre-flight calibration and initial data processing for the ChemCam laser-induced breakdown spectroscopy instrument on the Mars Science Laboratory rover. *Spectrochimica Acta Part B: Atomic Spectroscopy*, 82, 1–27. <https://doi.org/10.1016/j.sab.2013.02.003>
- Wiens, R. C., Maurice, S., & the MSL Science Team ChemCam (2015). Chemostratigraphy by the first Mars microprobe. *Elements*, 11(1), 33–38. <https://doi.org/10.2113/gselements.11.1.33>